scientific reports

Check for updates

OPEN

A hierarchical combination algorithm for real-time cycle slip detection and repair in low satellite elevation and high ionospheric activity conditions

Haofei Ban[1], Kezhao Li[1,2]✉, Kai Wang[1], Yingxiang Jiao[1], Lingfeng Liang[1], Chendong Tian[1] & Zhe Yue[1]

To enhance the accuracy and robustness of cycle slip detection and repair for triple-frequency data while minimizing the adverse effects of low satellite elevation and high ionospheric activity, a hierarchical combination algorithm for real-time cycle slip detection and repair is proposed. This algorithm begins by prioritizing the reduction of noise and ionospheric delay coefficients. It determines the optimal coefficients for the combination of observations from the BeiDou Navigation Satellite System's (BDS) Extra-Wide Lane (EWL), Wide Lane (WL), and Narrow Lane (NL). Leveraging the longer wavelength characteristics of the EWL combination, it simultaneously conducts cycle slip detection on the EWL combination alongside the pseudorange combination. Following this, based on the detection outcomes from the EWL combination, cycle slip detection is carried out on the WL combination. Finally, using the detection findings from the WL combination, cycle slip detection is executed on the NL combination. Given the NL combination's shorter wavelength and higher susceptibility to ionospheric delay, a dynamic ionospheric prediction model is applied to the NL combination to further mitigate the impact of ionospheric disturbances. After completing the cycle slip detection process, the results from the EWL, WL, and NL combinations are integrated and solved. Experimental results clearly demonstrate that, even in scenarios characterized by low satellite elevation and active ionospheric conditions, this algorithm consistently delivers outstanding detection performance for cycle slip instances, particularly for small cycle slip (less then two cycles). Remarkably, this performance is achieved without the need for intricate searches during cycle slip repair.

The BeiDou Navigation Satellite System (BDS) has injected fresh vigor into the advancement of Global Navigation Satellite Systems (GNSS). BDS boasts widespread applications in diverse domains such as aviation, maritime navigation, vehicle navigation, surveying, and geographic information systems[1–4]. Nevertheless, the practical use of GNSS receivers is often fraught with challenges due to the multitude of error sources during signal propagation. One such significant challenge is the cycle slip issue. A cycle slip denotes a sudden and discontinuous shift in the phase of satellite signals received by a GNSS receiver, stemming from various causes[5,6]. This phase disruption can result in inaccuracies in positioning, subsequently compromising navigation precision and dependability. To confront the cycle slip predicament, numerous researchers have put forth various cycle slip detection and repair methodologies. Common cycle slip detection approaches include those grounded in combination models, statistical features, and filtering techniques.

The cycle slip detection method based on combination models identifies cycle slips by skillfully amalgamating diverse models or multiple data sources to establish a comprehensive observation equation or parameter inversion model. This encompasses techniques such as the TurboEdit algorithm[7–9], the pseudorange phase combination method[10–12], and the ionospheric residual method[13–15], among others. The TurboEdit algorithm merges the Melbourne-Wübbena (MW) combination with the Geometry-Free (GF) combination, effectively mitigating

[1]School of Surveying and Land Information Engineering, Henan Polytechnic University, Jiaozuo 454000, China. [2]Collaborative Innovation Center of BDS Research Application, Zhengzhou 450052, China. ✉email: kz@hpu.edu.cn

the impact of insensitive cycle slips and delivering robust detection accuracy. Nevertheless, due to substantial pseudorange noise, the TurboEdit algorithm may struggle to detect small cycle slips lasting only 1–2 cycles; The pseudorange phase combination method is less susceptible to various errors and enjoys widespread adoption. However, due to the influence of ionospheric delay and pseudorange noise, it may not accurately detect small cycle slips, especially in situations with low elevation; The Phase Ionospheric Residual (PIR) method employs ionospheric combinations for cycle slip detection and repair, making it well-suited for identifying small cycle slips. However, in the presence of high ionospheric activity, the accuracy of cycle slip detection using this method may be compromised. Wang et al[16]. combined the GIGF combination and the quadratic difference between epochs to further improve the applicability of the TurboEdit algorithm during ionospheric active periods. However, the method is greatly affected by observation noise, and due to its uneven combination coefficients being integers, it requires the assistance of search algorithms in the cycle slip repair process. Huang et al[17]. proposed an instantaneous triple-frequency cycle slip detection and repair method that applies two geometry-free phase combinations and one geometry-free pseudorange minus phase linear combination for detecting insensitive cycle slips and uses the least-squares ambiguity decorrelation adjustment (LAMBDA) algorithm to search for cycle slip candidates. However, this method is susceptible to the influence of high ionospheric activity.

Statistical feature algorithms harness the statistical characteristics of signals, such as signal variance or higher-order moments, to pinpoint cycle slip events. These include techniques like wavelet transforms[18] and polynomial fitting methods[19–21], etc. The wavelet transform method is sensitive to small cycle slips but may exhibit reduced efficiency in cycle slip correction, making it less suitable for rapid processing; Huo et al[22]. studied the characteristics of non differential observation data and introduced SA4 wavelet to detect cycle slips, further improving the detection ability for small cycle slips. The polynomial fitting method detects cycle slips by fitting and calculating carrier phase sequence values, assessing whether the anomaly coincidence point signifies a cycle slip based on the consistency between the fitted curve and the measured curve. This method demands relatively high data sampling accuracy. Zhang et al[23]. used multiple time periods in the time difference model for cycle slip estimation and achieved good cycle slip repair results.

Filtering techniques employ filters to smooth signals and detect cycle slips by analyzing the residuals post-filtering. These encompass high-order differencing[24,25] and Kalman filtering[26,27], etc. High-order differencing stands out for its simplicity and absence of complex matrix operations, rendering it straightforward to implement. However, its detection process involves basic differencing and filtering, making it less suitable for identifying small cycle slips. Cai et al[28]. proposed an improved method that combined ionospheric residual and high-order difference. By combining the high-pass filtering characteristics of high-order differences and ionospheric residuals, the first-order difference is calculated to effectively suppress low-frequency signals and eliminate constant parts, amplifying the actual impact of cycle slips and improving the accuracy of cycle slip detection; Kalman filtering is an optimal filtering algorithm used to estimate the state of dynamic systems. While it can achieve high-precision cycle slip detection, it necessitates a high level of accuracy in system modeling and observational data quality. Liu et al[29]. employed the first-order Gauss–Markov stochastic process and Kalman filtering for real-time estimation. By conducting statistical hypothesis testing on predicted residual sequences, they successfully identified cycle slips, thereby enhancing the capability to detect such slips in various environmental conditions.

As GNSS technology continues its evolution, the introduction of new signal propagation environments and receiver technologies can pose fresh challenges concerning cycle slip occurrences. Hence, it becomes imperative to develop and fine-tune cycle slip detection and repair algorithms specifically tailored to these novel scenarios. How can it be more suitable for the use of the three types of BDS satellites in environments with low satellite elevation and high ionospheric activity? Alternatively, complex search steps can be omitted during cycle slip repair. In response to this need, a hierarchical combination for real-time cycle slip detection and repair has been introduced, with the primary objective of enhancing the precision and resilience of cycle slip handling in low satellite elevation and high ionospheric activity. Through comprehensive experimental validation and performance analysis, the efficacy of the proposed algorithm has been thoroughly examined and compared with existing methods. Research findings clearly demonstrate that the proposed algorithm maintains a high level of detection accuracy and correction precision, even in scenarios characterized by low satellite elevation and high ionospheric activity. This underscores its considerable potential for practical applications in challenging GNSS environments.

Theory and methods

BDS triple-frequency basic combination

The pseudorange and carrier observation equations for BDS are expressed as follows:

$$P_n = \rho + c(\delta T_r - \delta T) + \gamma_{P_n}\delta I_1 + trop + \varepsilon_{P_n} \tag{1}$$

$$l_n = \lambda_n\varphi_n = \rho + c(\delta T_r - \delta T) - \gamma_{\varphi_n}\delta I_1 + trop - \lambda_n N_n(t_0) + \varepsilon_{\varphi_n} \tag{2}$$

where:$n = 1, 2, 3$ denotes the different frequencies of BDS. For IGSO/MEO satellites, they represent the L1X, L5X, and L6I respectively, and for MEO satellites, they represent the L2I, L7D, and L6I respectively;ρ denotes the geometric distance between the receiver antenna and the satellite;c denotes the speed of light;δT_r and δT denote the receiver clock and the satellite clock, respectively;P and φ denote pseudorange observations and carrier phase observations, respectively;γ denotes the ionospheric delay coefficient;δI and $trop$ denote the ionospheric and the tropospheric delays, respectively; λ denotes carrier wavelength; $N(t_0)$ denotes ambiguity of whole cycles ;ε denotes observation noise. Combining three frequencies, the triple-frequency pseudorange and carrier combination can be represented respectively as:

$$P_{(a,b,c)} = aP_1 + bP_2 + cP_3 \tag{3}$$

$$l_{(i,j,k)} = [i \cdot f_1 \cdot \varphi_1 + j \cdot f_2 \cdot \varphi_2 + k \cdot f_3 \cdot \varphi_3]/f_{(i,j,k)} \tag{4}$$

where: f denotes the carrier frequency; (a, b, c) denote coefficients of the pseudorange combination; (i, j, k) denote coefficients of the carrier combination; $f_{(i,j,k)} = if_1 + jf_2 + kf_3$ denotes the frequency of the carrier combination.

To reduce errors, such as the receiver and satellite clock biases, differences are computed using observations between adjacent epochs[17]. The differences in pseudorange observations between adjacent epochs of Eq. (3) are expressed as:

$$\begin{aligned} \Delta P_{(a,b,c)} &= a\Delta P_1 + b\Delta P_2 + c\Delta P_3 \\ &= (a+b+c)(\Delta\rho + \gamma_{P(a,b,c)} \cdot \Delta\delta I^S + \sigma_{P(a,b,c)}) \end{aligned} \tag{5}$$

where: Δ denotes difference between adjacent epochs; γ_P denotes the ionospheric delay coefficients of pseudorange combination; σ_P denotes the noise of pseudorange combination.

The differences in carrier observations between adjacent epochs of Eq. (4) are expressed as

$$\begin{aligned} \Delta l_{(i,j,k)} &= [i \cdot f_1 \cdot \Delta\varphi_1 + j \cdot f_2 \cdot \Delta\varphi_2 + k \cdot f_3 \cdot \Delta\varphi_3]/f_{(i,j,k)} \\ &= \Delta\rho(t) - \gamma_{l(i,j,k)} \cdot \Delta\delta I_1 - \lambda_{(i,j,k)} \cdot \Delta N_{(i,j,k)}(t0) + \sigma_{l(i,j,k)} \end{aligned} \tag{6}$$

where: γ_l denotes the ionospheric delay coefficients of carrier combination; $\lambda_{(i,j,k)}$ denotes the wavelength of the carrier combination; $N_{(i,j,k)}(t_0)$ denotes the ambiguity of carrier combination. σ_l denotes the noise of carrier combination.

The specific expressions for each of these quantities are as shown in Table 1:

In order to find the optimal linear combination of carriers, it is essential to establish effective selection criteria. As per Eq. (6), the residual ionospheric delay and observation noise play a crucial role in determining phase ambiguities. Taking into consideration the different combination wavelengths, the following two criteria are adopted: (1)Minimize the ionospheric delay coefficients to reduce the impact of ionospheric variability; (2)Minimize the interference of observation noise on data as much as possible. These criteria can be expressed as follows:

$$\begin{cases} (i,j,k) = \underset{(i,j,k)}{\arg\min} \left(\left| \frac{\gamma_{l(i,j,k)}}{\lambda_{(i,j,k)}} \right| \right) \\ (i,j,k) = \underset{(i,j,k)}{\arg\min} \left(\left| \frac{\sigma_{l(i,j,k)}}{\lambda_{(i,j,k)}} \right| \right) \end{cases} \tag{7}$$

Based on the geometric analysis in reference[30], simultaneously mitigating errors caused by observation noise and ionospheric delay presents a set of conflicting factors. Therefore, in practice, there is a need to strike a balance between these two factors by selecting suitable combination coefficients through a compromise. To limit the error magnitude, integer coefficients should be determined within the range of − 5 to 5. Assuming that the carrier observation noise for the three frequencies is independently and identically distributed with the same standard deviation[31,32], and given that the carrier phase noise for different BDS frequency bands is the same(i.e.,$\varepsilon_{\varphi_1} = \varepsilon_{\varphi_2} = \varepsilon_{\varphi_3} = 0.002m$),the coefficients $l_{(0,-1,1)}$, ,$l_{(1,0,-1)}$ and $l_{(1,0,0)}$ are selected as the best combination based on the selection criteria. The BDS carrier frequencies are L1X, L2I, L5X, L6I, and L7D, with IGSO/MEO satellites using L1X, L5X, and L6I frequencies, and GEO satellites using L2I, L7D, and L6I frequencies. The Extra-Wide Lane (EWL), Wide Lane (WL), and Narrow Lane (NL) combinations parameters for the three-frequency BDS signals are as shown in Table 2.

$\lambda_{(i,j,k)} = \frac{c}{f_{(i,j,k)}}$	$\gamma_{P(a,b,c)} = a + b \cdot \frac{f_1^2}{f_2^2} + c \cdot \frac{f_1^2}{f_3^2}$
$\gamma_{l(i,j,k)} = \frac{f_1}{f_{(i,j,k)}}(i + j\frac{f_1}{f_2} + k\frac{f_1}{f_3})$	$\sigma^2_{P(a,b,c)} = a^2\varepsilon^2_{P_1} + b^2\varepsilon^2_{P_2} + c^2\varepsilon^2_{P_3}$
$\sigma^2_{l(i,j,k)} = \frac{i^2f_1^2\varepsilon^2_{\varphi_1} + j^2f_2^2\varepsilon^2_{\varphi_2} + k^2f_3^2\varepsilon^2_{\varphi_3}}{f^2_{(i,j,k)}}$	$\Delta N_{(i,j,k)}(t0) = iN_1(t0) + kN_2(t0) + jN_3(t0)$

Table 1. Symbolic meaning.

Satellite type	Combination type (i, j, k)	γ_l	σ_l	$\lambda_{(i,j,k)}(m)$
GEO (IGSO/MEO)	EWL (0, − 1,1)	− 1.591 (− 1.663)	0.057 (0.037)	4.884 (3.256)
	WL (1,0, − 1)	− 1.293 (− 1.241)	0.011 (0.013)	0.846 (0.976)
	NL (1,0,0)	1.000 (1.000)	0.002 (0.002)	0.192 (0.190)

Table 2. Linear combination of triple frequency BDS signals.

According to Eq. (5), pseudorange combination is primarily affected by pseudorange observation noise. Similar to carrier observation noise[33], assume that the pseudorange noise for BDS is the same (i.e.,$\varepsilon_{P_1} = \varepsilon_{P_2} = \varepsilon_{P_3} = \varepsilon_P = 0.3m$). Referring to Table 1, it is apparent that when $a = b = c = 1/3$, the combination noise is minimized. Therefore, selecting $P_{(1/3,1/3,1/3)}$ as the pseudorange combination coefficient. After determining the coefficients for carrier and pseudorange combination, a hierarchical combination model is established to facilitate cycle slip detection and repair.

The hierarchical combination model

EWL combination cycle slip detection model

The EWL combination retains the integer cycle slips of the combination ambiguity, and since the wavelength is large, it is not affected much by the residual errors. First, cycle slips of the EWL combination are detected and repaired. Combined with the pseudorange combination, the pseudorange and carrier phase combination is constructed according to Eqs. (5) and (6), which is expressed as:

$$\begin{aligned}\Delta N_{(0,-1,1)} &= \Delta l_{(0,-1,1)} - \Delta P_{(1/3,1/3,1/3)} \\ &= \left[(f_2\Delta\varphi_2 - f_3\Delta\varphi_3)/(f_2 - f_3) - (\Delta P_1 + \Delta P_2 + \Delta P_3)/3\right]/\lambda_{(0,-1,1)} + \eta_1\Delta\delta I_1 + \sigma_1\end{aligned} \tag{8}$$

$$\begin{cases}\eta_1 = -(\gamma_{(0,-1,1)} + \gamma_{(1/3,1/3,1/3)})/\lambda_{(0,-1,1)} \\ \sigma_1 = \sqrt{\sigma^2_{P_{(1/3,1/3,1/3)}} + \sigma^2_{l_{(0,-1,1)}}}/\lambda_{(0,-1,1)}\end{cases} \tag{9}$$

The ionospheric coefficients η_1 for GEO satellites and IGSO/MEO satellites in the EWL combination are 0.040 and 0.066, respectively. Correspondingly, the observation noise values σ_1 are 0.037 and 0.054, respectively. When the EWL combination observation exceeds 0.5, indicating that $\left|\Delta N_{(0,-1,1)}\right| > 0.5$, it is considered a cycle slip. In such instances, the cycle slip value for the EWL combination is simply rounded to the nearest integer, denoted as $\Delta\hat{N}_{(0,-1,1)} = round[\Delta N_{(0,-1,1)}]$. Given the negligible magnitude of η_1, it can effectively be disregarded when using a 30 s sampling interval[31]. Consequently, the success rate of cycle slip detection for the EWL combination is as follows:

$$\begin{aligned}P_1 &= P\left(\left|\Delta N_{(0,-1,1)} - \Delta\hat{N}_{(0,-1,1)}\right| < 0.5\right) \\ &= \Phi\left(\frac{0.5 - \eta_1\cdot\Delta\delta I_1}{\sigma_1}\right) + \Phi\left(\frac{0.5 + \eta_1\cdot\Delta\delta I_1}{\sigma_1}\right) - 1 = 100\%\end{aligned} \tag{10}$$

WL combination cycle slip detection model

After the cycle slip of the EWL combination is determined, the repaired EWL combination is utilized to detect the observations of the WL combination:

$$\Delta N_{(1,0,-1)} = \frac{1}{\lambda_{(1,0,-1)}}(\Delta l_{(1,0,-1)} - \Delta l_{(0,-1,1)} + \lambda_{(0,-1,1)}\Delta\hat{N}_{(0,-1,1)}) + \eta_2\Delta\delta I_1^S + \sigma_2 \tag{11}$$

$$\begin{cases}\eta_2 = (-\gamma_{(1,0,-1)} + \gamma_{(0,-1,1)})/\lambda_{(1,0,-1)} \\ \sigma_2 = \sqrt{\sigma^2_{l_{(1,0,-1)}} + \sigma^2_{l_{(0,-1,1)}}}/\lambda_{(1,0,-1)}\end{cases} \tag{12}$$

The ionospheric coefficients η_2 for GEO satellites and IGSO/MEO satellites in the WL combination are -0.352 and -0.431, respectively. Correspondingly, the observation noise values σ_2 are 0.068 and 0.040 respectively. When the WL combination observation exceeds 0.5, indicating that $\left|\Delta N_{(1,0,-1)}\right| > 0.5$, it is considered a cycle slip. In such instances, the cycle slip value for the WL combination is simply rounded to the nearest integer, denoted as $\Delta\hat{N}_{(1,0,-1)} = round[\Delta N_{(1,0,-1)}]$.Similarly to the EWL combination, since the η_2 value remains small, it can be ignored with a 30 s sampling interval for WL combination. Therefore, the success rate of cycle slip detection for the WL combination is:

$$\begin{aligned}P_2 &= P\left(\left|\Delta N_{(1,0,-1)} - \Delta\hat{N}_{(1,0,-1)}\right| < 0.5\right) \\ &= \Phi\left(\frac{0.5 - \eta_2\cdot\Delta\delta I_1}{\sigma_2}\right) + \Phi\left(\frac{0.5 + \eta_2\cdot\Delta\delta I_1}{\sigma_2}\right) - 1 = 100\%\end{aligned} \tag{13}$$

NL combination cycle slip detection model

After the cycle slip of the WL combination is determined, the repaired WL combination is utilized to detect the observations of the NL:

$$\Delta N_{(1,0,0)} = \frac{1}{\lambda_{(1,0,0)}}(\Delta l_{(1,0,0)} - \Delta l_{(1,0,-1)} + \lambda_{(1,0,-1)}\Delta\hat{N}_{(1,0,-1)}) + \eta_3\cdot\Delta\delta I_1 + \sigma_3 \tag{14}$$

$$\begin{cases} \eta_3 = (-\gamma_{(1,0,0)} + \gamma_{(1,0,-1)})/\lambda_{(1,0,0)} \\ \sigma_3 = \sqrt{\sigma^2_{(1,0,0)} + \sigma^2_{(1,0,-1)}}/\lambda_{(1,0,0)} \end{cases} \tag{15}$$

The ionospheric coefficients η_3 for GEO satellites and IGSO/MEO satellites in the NL combination are − 11.941 and − 11.781, respectively. The observation noise values σ_3 are 0.058 and 0.070, respectively. It is evident that when the value of η_3 experiences a significant increase, direct integer rounding of NL's cycle slip values may not be suitable during periods of heightened ionospheric activity. Polynomial regression models are commonly employed to capture temporal variations. In this context, a polynomial regression function incorporating time variables can be introduced to model the time series of NL combination values. This facilitates the prediction of epoch-to-epoch ionospheric delay within the NL combination, thereby mitigating the influence of ionospheric delay. The general form of a polynomial regression fit with a window size of n and a polynomial order of p is as follows:

$$\begin{cases} y(t) = x_0 + x_1\Delta t(1) + x_2\Delta t(2)^2 + \cdots + x_p\Delta t(i)^p \\ \Delta t(i) = t_i - t_{i-1} \end{cases} \tag{16}$$

where: $i = 1, 2, 3, \cdots, m$;x and y denote polynomial regression coefficients and NL combination observations, respectively. t denotes the time of the epoch. The choice of the polynomial fit order p in polynomial regression should be based on the variations of each NL combination value with respect to time within the data cycle. According to prior research: During periods of active ionospheric conditions, p is set to 2. And during stable ionospheric conditions, p is set to 1[34]. The decreasing correlation between observations over time has been confirmed through multiple tests. It has been found that a time interval of 5 to 15 min is sufficient to meet the requirements of the prediction window under normal conditions. However, when satellite elevation is relatively low, and noise effects are more pronounced, longer time intervals are needed for prediction. Therefore, in the calculation of ionospheric delay, a dynamic window of length m is employed, with the maximum window size set to $m_{\max} = 30$. The specific implementation strategy is as follows:

(1) When the receiver initially receives satellite signals, especially when the satellite elevation is low, and effective data support is needed for subsequent NL combination observations detection, the window size should be as large as possible. Therefore, in this case, the window size is set to the maximum window count, which is $m = m_{\max}$;
(2) When the satellite elevation EL is greater than 30°, the variations in multipath error and noise error tend to be relatively smooth. Therefore, in this situation, it is advisable to use a fixed window size for data processing, which is typically expressed as $m = 0.5m_{\max}$.
(3) When EL is less than 30° but greater than 15°, where noise error has a significant impact, it is advisable to dynamically adjust the window size to better accommodate the changing elevation. In this case, the window size can be set as $m = m_{\max}(1 - \sin el)$.
(4) When EL is less than 15°, noise error significantly increases, and in such conditions, it is advisable to use the maximum window size. Additionally, when EL is less than 10°, it becomes challenging to capture satellite signals, and the signal quality is very poor. Therefore, for EL less than 15° greater than 10° the window size can be set as $m = m_{\max}$.

In summary, the dynamic window size can be expressed as follows:

$$m = \begin{cases} m_{\max}\ i \le m_{\max} \\ 0.5m_{\max}\ EL \ge 30°, i > m_{\max} \\ m_{\max}(1 - \sin el)\ 15° \le EL < 30°, i > m_{\max} \\ m_{\max}\ 10° \le EL < 15°, i > m_{\max} \end{cases} \tag{17}$$

After determining the order of polynomial fitting and the window, the following equation can be derived based on Eq. (16):

$$\begin{pmatrix} 1 & \Delta t(i-m+1) & \cdots & (\Delta t(i-m+1))^p \\ 1 & \Delta t(i-m+2) & \cdots & (\Delta t(i-m+2))^p \\ \vdots & \vdots & \vdots & \vdots \\ 1 & \Delta t(i) & \cdots & (\Delta t(i))^p \end{pmatrix} \begin{pmatrix} x_0 \\ x_1 \\ \vdots \\ x_p \end{pmatrix} = \begin{pmatrix} \Delta N_{(1,0,0)}(i-m+1) \\ \Delta N_{(1,0,0)}(i-m+2) \\ \vdots \\ \Delta N_{(1,0,0)}(i) \end{pmatrix} \tag{18}$$

Equation (18) can be simplified into matrix form as $\boldsymbol{A}_{NL}\boldsymbol{X}_{NL} = \boldsymbol{Y}_{NL}$. Subsequently, the error equation matrix can be expressed as $\boldsymbol{V}_{NL} = \boldsymbol{A}\boldsymbol{X}_{NL} - \boldsymbol{Y}_{NL}$. Employing the least squares principle and the function-free extrema algorithm, we can eliminate $\boldsymbol{V}_{NL}$ to obtain the polynomial fitting coefficients $\hat{\boldsymbol{X}}_{NL}$, denoted as:

$$\hat{\boldsymbol{X}}_{NL} = (\boldsymbol{A}^{\mathrm{T}}_{NL}\boldsymbol{A}_{NL})^{-1} - \boldsymbol{A}^{\mathrm{T}}_{NL}\boldsymbol{Y}_{NL} \tag{19}$$

After obtaining the polynomial fitting coefficients, the predicted ionospheric layer delay of the $(m+1)$th epoch can be expressed as:

$$I_{NL}(i_{m+1}) = \hat{x}_0 + \hat{x}_1\Delta t(i_{m+1}) + \hat{x}_2\Delta t(i_{m+1})^2 + \cdots + \hat{x}_p\Delta t(i_{m+1})^p \tag{20}$$

At the same time, in order to ensure the accuracy of ionospheric prediction results, it should be ensured that there is no cycle slip in the data within the initial window. The judgment algorithm is as follows:

(1) According to the Eq. (19), obtain the polynomial fitting coefficients $\overline{\boldsymbol{X}}_{NL} = \left[\begin{array}{cccc} \overline{x}_0 & \overline{x}_1 & \cdots & \overline{x}_p \end{array}\right]^{\mathrm{T}}$ within the initial window, then the predicted ionospheric delay $\overline{I}_{NL}$ within the initial window can be expressed as $\overline{I}_{NF}(i) = \overline{x}_0 + \overline{x}_1 \Delta t(i) + \overline{x}_2 \Delta t(i)^2 + \cdots + \overline{x}_p \Delta t(i)^p$;
(2) If the NL combination observations within the initial window satisfy:$|\Delta N_{(1,0,0)} - \overline{I}_{NF}(i)| < 0.5$.

Finally, the cycle slip value of NL combination can be expressed as:

$$\Delta \hat{N}_{(1,0,0)} = round[\Delta N_{(1,0,0)} - I_{NL}] \tag{21}$$

Cycle slip repair
Solving for cycle slips $\hat{N}$ on three frequencies using the hierarchical combination model:

$$\begin{pmatrix} 0 & -1 & 1 \\ 1 & 0 & -1 \\ 1 & 0 & 0 \end{pmatrix} \begin{pmatrix} \hat{N}_1 \\ \hat{N}_2 \\ \hat{N}_3 \end{pmatrix} = \begin{pmatrix} \Delta \hat{N}_{(0,-1,1)} \\ \Delta \hat{N}_{(1,0,-1)} \\ \Delta \hat{N}_{(1,0,0)} \end{pmatrix} \tag{22}$$

Simplify Eq. (20) into matrix form $\boldsymbol{AX} = \boldsymbol{Y}$. Since the combination coefficients and the obtained cycle slip values are integers, the rank of $\boldsymbol{A}$ is 3, multiply $\boldsymbol{A}^{-1}$ directly to obtain the cycle slip values, i.e.,$\boldsymbol{X} = \boldsymbol{A}^{-1}\boldsymbol{Y}$.
The flowchart of the entire algorithm is shown in Fig. 1.

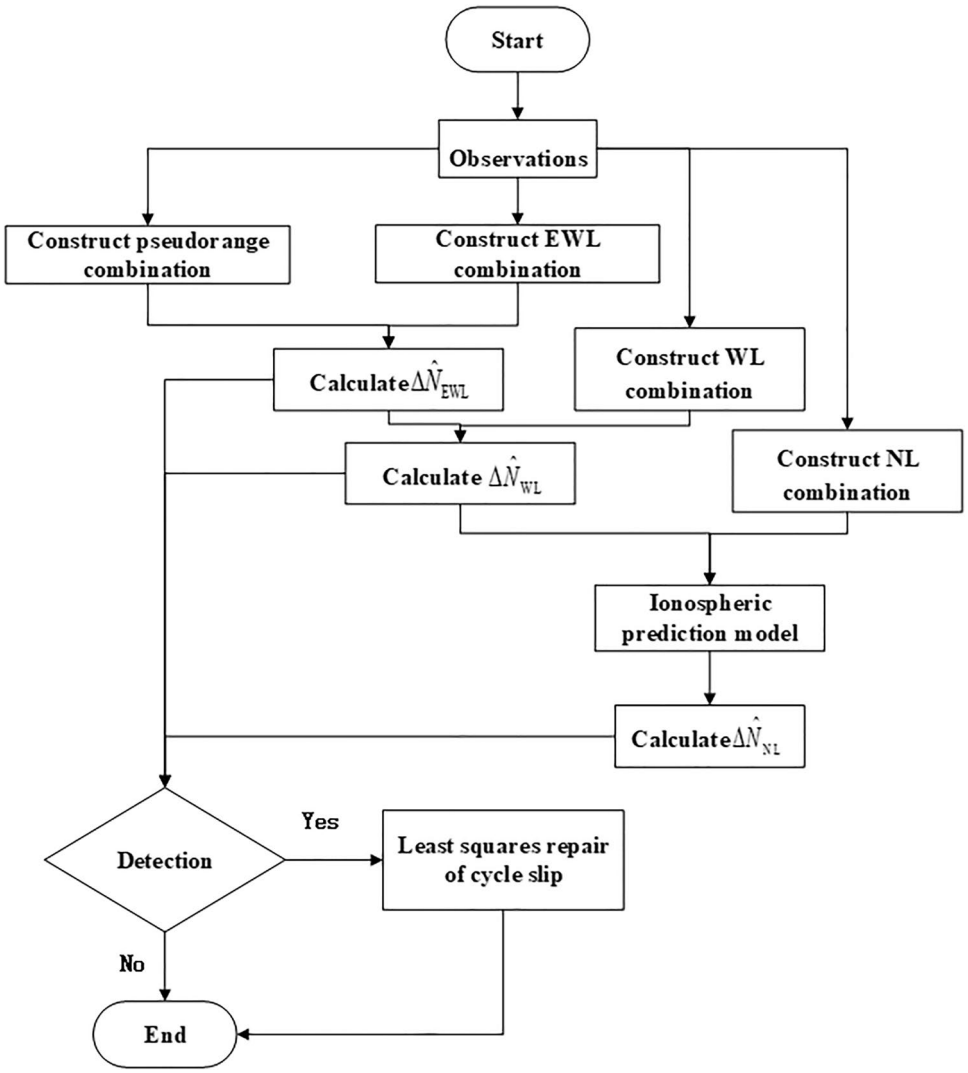

Figure 1. Flowchart of the cycle slip detection and repair algorithm.

Results and discussion

The data comes from the IGS WUH2 station TRIMBLE ALLOY GNSS station receiver. The collection time is September 04, 2022, and the sampling rate is 30 s. A total of 2880 epochs of BeiDou satellite observation data were selected for experimental analysis. The geomagnetic Kp index on the day of the experimental data was obtained from the Space Environment Prediction Center (http://www.sepc.ac.cn) as shown in Fig. 2:

According to the calculation, the average Kp index on September 4, 2022 is 4.75, exceeding 5 most of the time, which means a major geomagnetic storm occurred that day and the ionosphere was in a violent activity state.

The experiment is divided into two schemes, as follows:

Scheme I: Verify with the original station data. The algorithm of hierarchical combination cycle slip detection and repair (hereinafter referred to as Algorithm 1) is directly used to detect and repair cycle slips in the original data, and compared with the three-frequency Geometry-Free and Ionosphere-Free(GFIF) combination algorithm (hereinafter referred to as Algorithm 2) detection and repair results in Reference[16] to verify the basic performance of Algorithm 1. Algorithm 2 incorporates MW combination, GIGF combination, and PIR combination, building upon the TurboEdit algorithm, which is currently one of the most widely used cycle slip detection algorithms. In order to further ensure the accuracy of the Algorithm 2 for cycle slip repair, the least-squares ambiguity decorrelation adjustment (LAMBDA)[17] is used to search for cycle slip candidates of the Algorithm 2. Because for a carrier data segment, the type of cycle slips occurred is singular. To further verify the applicability of Algorithm 1 to various types of cycle slips, obtain the carrier data without cycle slips through Scheme 1 for the next experiment.

Scheme II: Taking the carrier data without cycle slips from Scheme I as the basis, first add different types of cycle slip combinations from the $(m_{\max} + 1)$th epoch of the carrier data at intervals of 5 epochs. The first 8 cycle slip combinations are insensitive small cycle slips of EWL, WL or NL combinations, which are (1,0,0), (0,1,0), (0,0,1), (0, 2, 2), (3, 0, 3), (5, 4, 0), (5, 5, 5) and (13, 10, 0). Other cycle slip combinations are random cycle slip combinations of 0–9 cycles randomly generated for each frequency (not all zeros for the 3 frequencies). Algorithm 1 and Algorithm 2 are used to detect and repair cycle slips in the experimental data, with the purpose of fully verifying the correctness, effectiveness and applicability of Algorithm 1 in detecting and repairing different cycle slip combinations (especially insensitive cycle slips).

Results and analysis of scheme 1

Figure 3 shows the detection results of Algorithm 1 for satellites C19, C38, and C59. It can be seen from Fig. 3 that the EWL combination is not affected by the satellite elevation and ionosphere, and the combination observations are within the detection threshold range without significant fluctuations. The WL combination is not affected by the ionosphere. Due to the influence of satellite elevation, the fluctuation amplitude of the combination observation increases at low elevation, but the fluctuation range is still within the detection threshold. The NL combination is affected by both elevation and ionosphere, so the fluctuation range of the combination observations changes dramatically, with a considerable portion exceeding the detection threshold. However, the NL combination improved by the dynamic ionospheric prediction model is not affected by elevation and ionosphere. Its combination observations are within the detection threshold range without significant fluctuations.

Figure 4 shows the detection results of Algorithm 2 for satellites C19, C38, and C59. It can be seen from Fig. 4 that the GFIF combination is not affected by satellite elevation and ionosphere. The combination observations are within the detection threshold range without significant fluctuations. The MW combination is not affected by the ionosphere. Due to the severe influence of satellite elevation, the fluctuation range of the combined values increases significantly at low elevation, with some exceeding the threshold. The PIR combination has an obviously larger fluctuation range in the combination observations due to the dual influence of elevation and ionosphere, and some of the combination observations exceed the detection threshold.

The cycle slip detection results of Algorithm 1 are shown in Table 3. Algorithm 1 did not detect cycle slips on satellites C19 and C59, and detected one group of cycle slips on satellite C38 which can be corrected successfully, without false detection. The unimproved algorithm (without using ionospheric prediction model), a total of 183 sets of cycle slips were detected, and none of them were successfully repaired. Therefore, the ionospheric

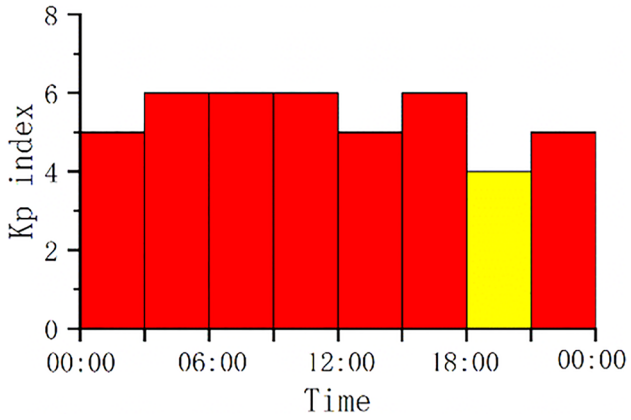

Figure 2. Geomagnetic Kp index.

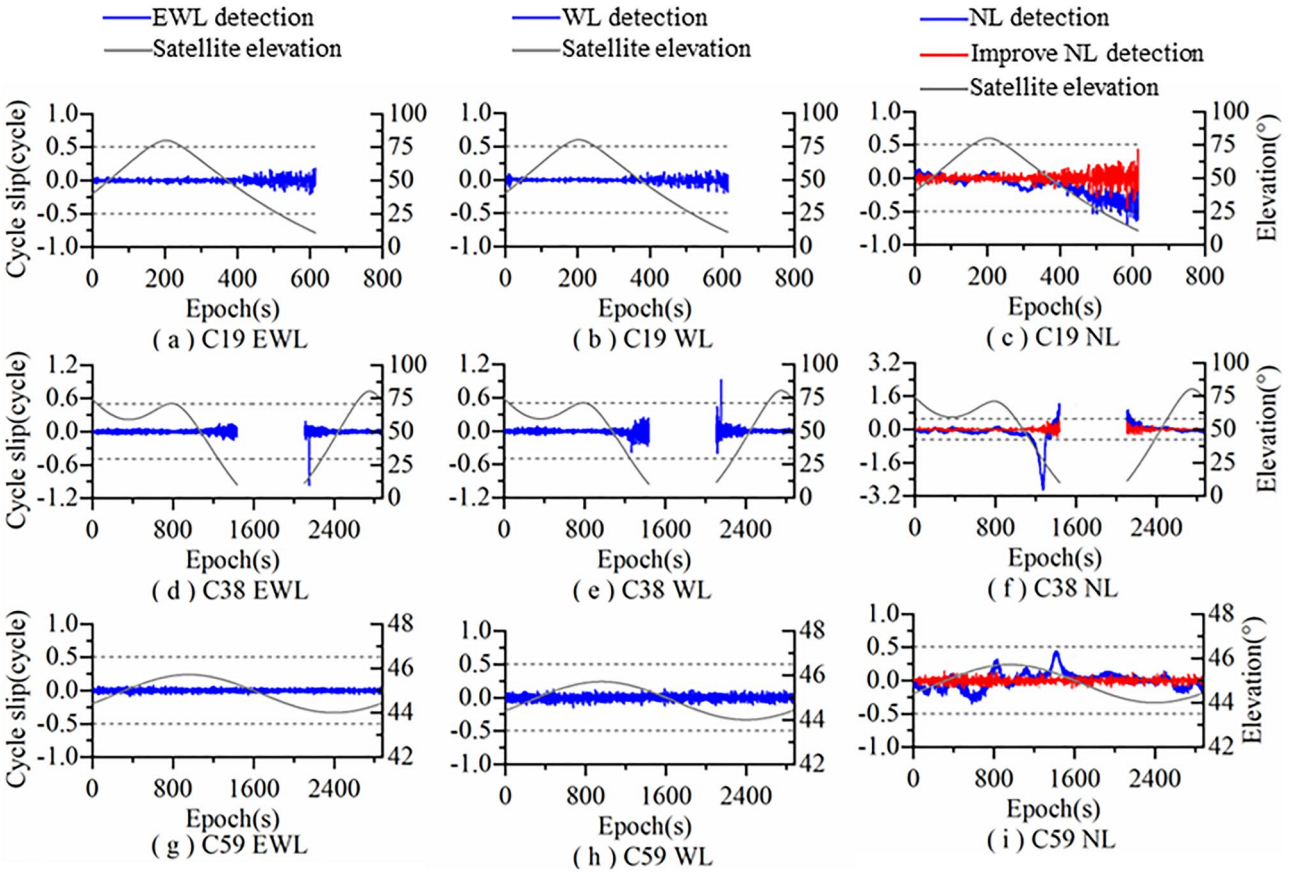

Figure 3. Algorithm 1 cycle slip detection results.

prediction model can effectively weaken the impact of ionospheric activity on NL combinations, further improving the accuracy of cycle slip detection and repair.

The cycle slip detection results of Algorithm 2 in are shown Table 4. Algorithm 2 did not detect cycle slips on satellite C59. It detected 17 groups of cycle slips on C19 and C38, but only one set of cycle slip was successfully fixed, and the rest failed to be fixed, resulting in false detection.

Therefore, compared with Algorithm 2, Algorithm 1 has higher accuracy and better applicability in cycle slip detection and repair. After the measured data was repaired by Algorithm 1, the changes of all combination observations were within the detection threshold. The cycle slip detection figures after repair are not shown due to limited space.

Results and analysis of scheme II

Figure 5 shows the detection results of Algorithm 1 for simulated cycle slips added to satellites C19, C38 and C59. It can be seen from Fig. 5 that in Algorithm 1, the EWL combination is insensitive to combined cycle slips like (1,0,0), (0,2,2) and (5,5,5), but can detect other combined cycle slips. The WL combination is insensitive to combined cycle slips like (0,1,0), (3,0,3) and (5,5,5), but can detect other combined cycle slips. The NL combination is insensitive to combined cycle slips like (0,1,0), (0,0,1), (0,2,2) and (3,0,3), but can detect other combined cycle slips. Therefore, by combining EWL, WL and NL, Algorithm 1 can detect all the added simulated cycle slips and there are no undetectable insensitive cycle slips.

Figure 6 shows the detection results of Algorithm 2 for simulated cycle slips added to satellites C19, C38 and C59. It can be seen from Fig. 6 that in Algorithm 2, GFIF combination is insensitive to the combined cycle slips (1,0,0), (0,2,2) and (5,5,5), but can detect other combined cycle slips. The MW combination is insensitive to the combined cycle slips (0,1,0), (3,0,3) and (5,5,5). At the same time, due to the influence of satellite elevation, it still cannot accurately detect the remaining cycle slip combinations. The PIR combination is insensitive to the combined cycle slip (13,10,0), but still cannot detect all the remaining cycle slip combinations due to the influence of ionospheric activity. Therefore, by combining GFIF, MW and PIR, Algorithm 2 can also detect the added simulated cycle slips, but there will be false detections.

The repair results of simulated cycle slips by Algorithm 1 are shown in Table 5. Statistically, Algorithm 1 can correctly repair all the 1123 groups of simulated cycle slips added to the 3 satellites, especially for insensitive small cycle slip combinations, with a 100% correction accuracy.

The repair results of simulated cycle slips by Algorithm2 are shown in Table 6. Among the 1123 groups of simulated cycle slips added to the 3 satellites, Algorithm 2 correctly repaired 1113 groups and incorrectly repaired

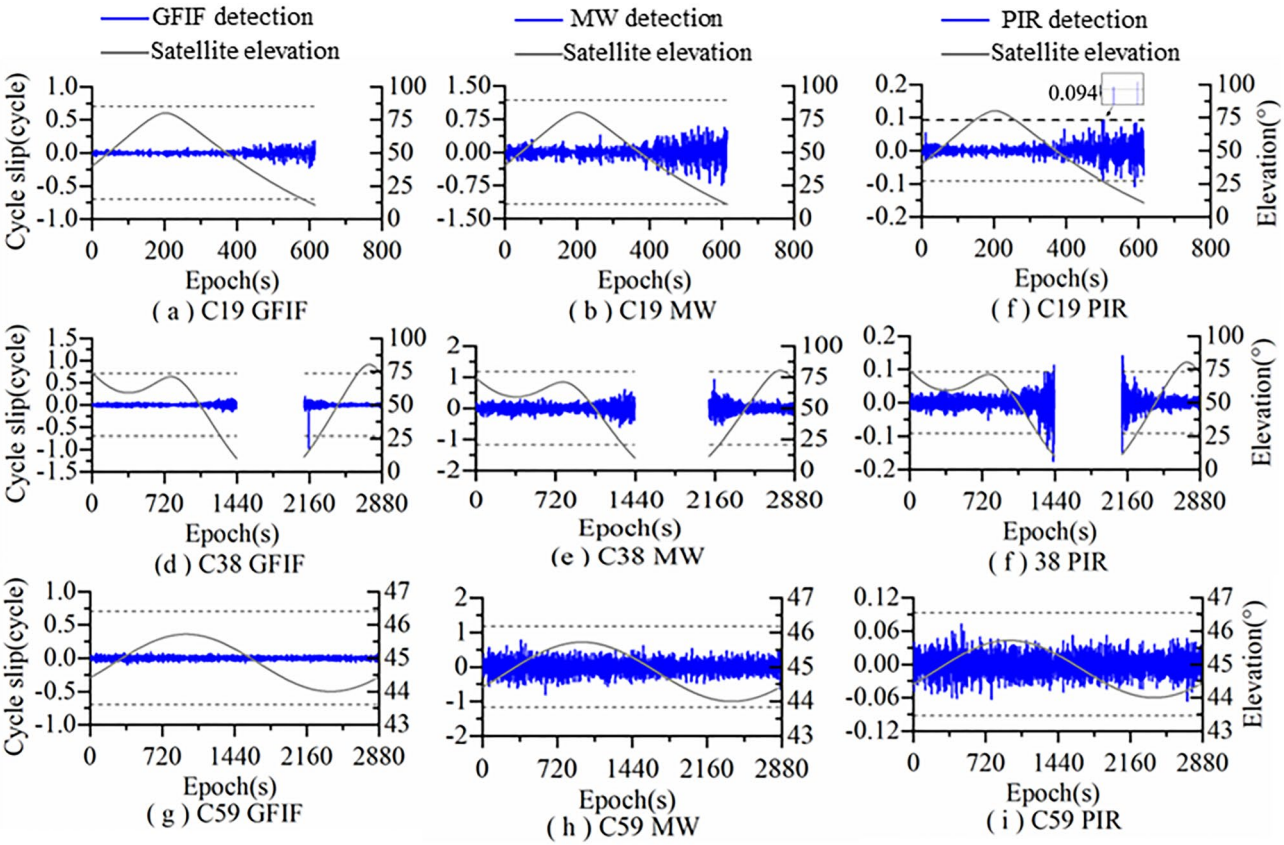

Figure 4. Algorithm 2 cycle slip detection results.

Algorithm	Satellite	Cycle slips	Successfully repaired	Failed repaired
Algorithm 1 (Without improving)	C19- MEO	/ (12)	/ (0)	/ (12)
	C38-IGSO	1 (171)	1 (0)	0 (171)
	C59-GEO	/ (/)	/ (/)	/ (/)

Table 3. Results of using Algorithm 1 to detect and repair cycle slip for the original data.

Algorithm	Satellite	Cycle slips	Successfully repaired	Failed repaired
Algorithm 2 (Without LAMBDA)	C19-MEO	2 (2)	0(0)	2 (2)
	C38- IGSO	15 (15)	1 (0)	14 (15)
	C59-GEO	/ (/)	/ (/)	/ (/)

Table 4. Results of using Algorithm 2 to detect and repair cycle slip for the original data.

10 groups, with a correction accuracy of 99.1%. Algorithm 2 without MLABDA correctly repaired 649 groups and incorrectly repaired 474 groups, with a correction accuracy of 57.79%.

Comparing Algorithm 2, Algorithm 1 adopts hierarchical cycle slip detection and ionospheric prediction model to improve the accuracy of cycle slip detection while avoiding the complex search process in the traditional combination model for cycle slip repair, thus improving the correctness of cycle slip repair. Due to the fact that the combination coefficients of Algorithm 1 are all integers, there is no need for complex searches to ensure the accuracy of cycle slip repair.

Conclusions

In this paper, an optimized algorithm for real-time hierarchical combination cycle slip detection and repair is proposed, which is not restricted by active ionospheric conditions. By using EWL, WL and NL combination models, cycle slips can be reliably detected and repaired under good conditions. However, successfully detecting

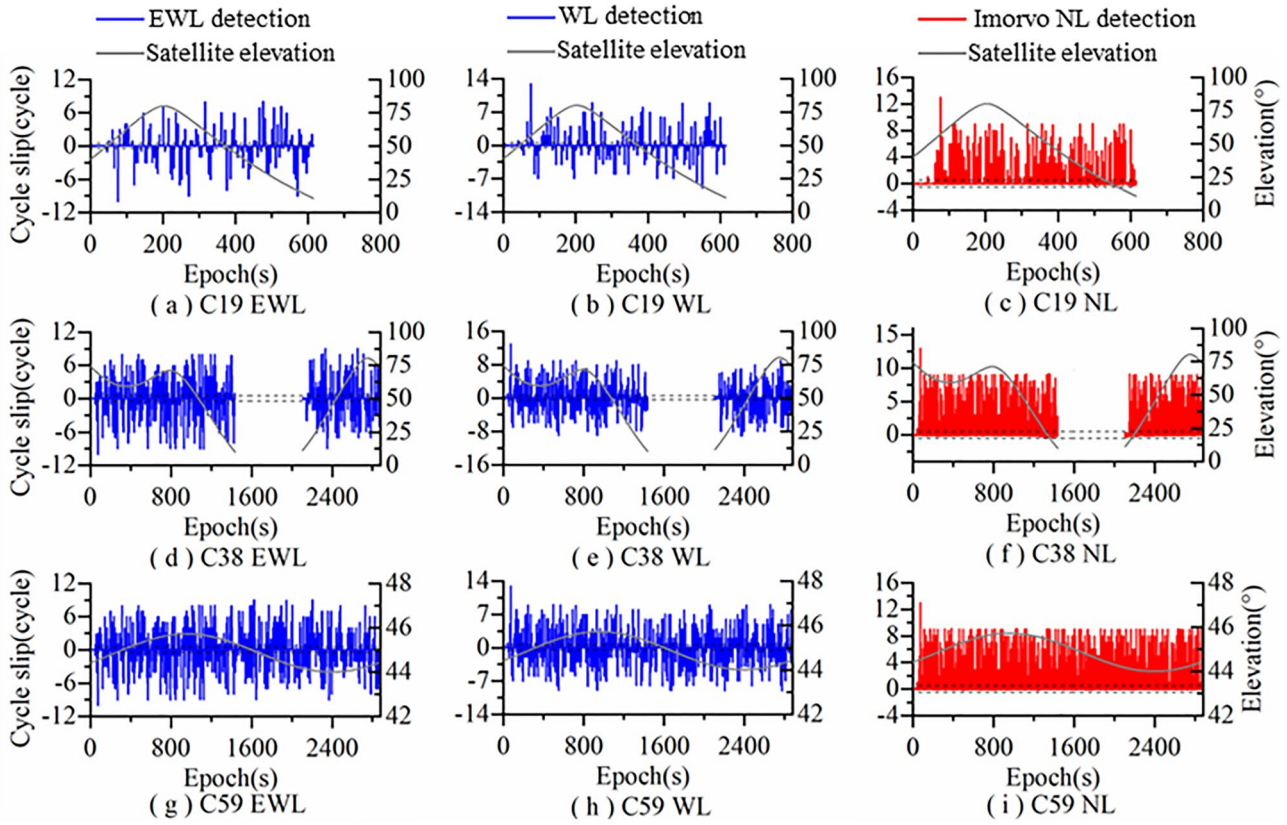

Figure 5. Simulated cycle slip detection results of Algorithm 1.

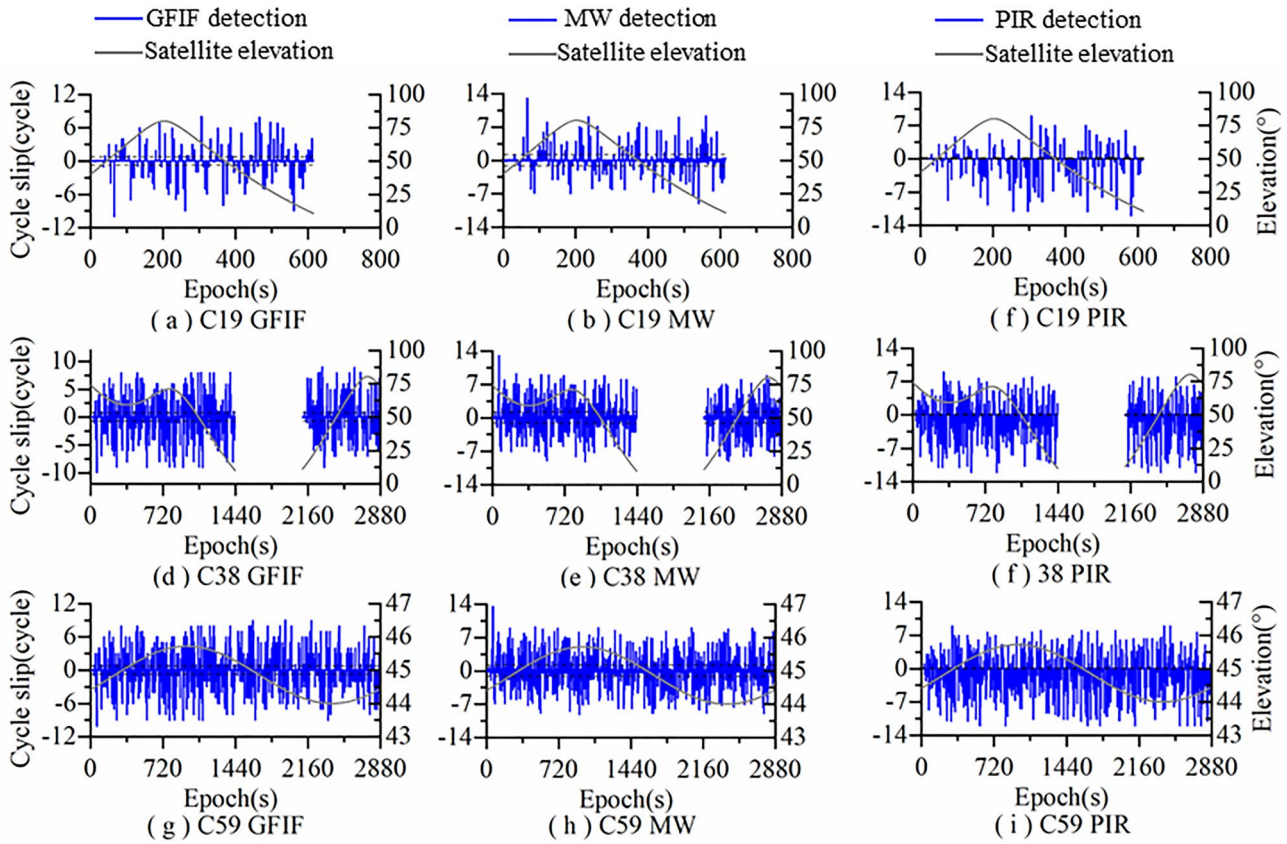

Figure 6. Simulated cycle slip detection results of Algorithm 2.

Algorithm	Satellite	Cycle slips	Successfully repaired	Failed repaired
Algorithm 1	C19-MEO	118	118	0
	C38- IGSO	434	434	0
	C59-GEO	571	571	0

Table 5. Simulated cycle slip repair results of Algorithm 1.

Algorithm	Satellite	Cycle slips	Successfully repaired	Failed repaired
Algorithm 2 (Without LAMBDA)	C19-MEO	118	116 (59)	2 (59)
	C38- IGSO	434	429 (263)	5 (171)
	C59-GEO	571	568 (327)	3 (244)

Table 6. Simulated cycle slip repair results of Algorithm 2.

and repairing cycle slips is challenging under low elevation and/or active ionospheric conditions. The newly proposed algorithm improves the cycle slip detection performance by incorporating the predicted epoch-differenced ionospheric delays to construct an ionospheric prediction model, in order to increase the accuracy of estimating cycle slip integer values.

The algorithm has many advantages. Firstly, it can detect all small cycle slips including insensitive ones. Secondly, even with rapidly varying ionospheric delays, the algorithm can still predict the ionospheric differences between epochs through the ionospheric prediction model to resolve false detections. Finally, the algorithm does not require complex search during cycle slip repair and can achieve efficient cycle slip detection and real-time repair with good accuracy and robustness.

The experimental results show that even during ionospherically active periods, the algorithm still has good detection performance for insensitive cycle slip combinations, especially small-cycle combinations. Also, during the cycle slip repair process, the algorithm can complete the repair without complex search.

Our future research will primarily focus on two crucial areas. Firstly, we intend to broaden our exploration to multiple satellite systems, such as GPS and Galileo. Simultaneously, we have observed that the positioning principles of BDS, GPS, and Galileo share a fundamental similarity. With the exception of BDS's GEO satellites, the basic principles of other satellite systems align, providing a foundation for our approach to achieve consistent performance across different systems. This expansion aims to deepen our understanding of the versatility and effectiveness of our methodology across various satellite constellations. Secondly, we aim to assess how our approach performs in more disrupted ionospheric conditions, evaluating its resilience in intricate environments. These efforts are directed towards continually refining and advancing the cycle-slip detection technique, ensuring its adaptability across diverse satellite systems. This adaptability is crucial for the algorithm to consistently deliver stable and accurate performance in real-world applications, particularly in the face of challenging ionospheric scenarios.

Data availability

The authors confirm that the data supporting the findings of this study are available within the article and its supplementary materials. The supplementary materials include simulation data from the experiments and details on how to obtain them are provided in the file description document.

Received: 11 September 2023; Accepted: 24 January 2024
Published online: 29 January 2024

References

1. Wang, E. *et al.* Evaluation of BDS/GPS multi-frequency RTK Positioning performance under different baseline lengths. *Remote Sens.* **14**(15), 3561 (2022).
2. Lv, J. *et al.* Modeling and assessment of multi-frequency GPS/BDS-2/BDS-3 kinematic precise point positioning based on vehicle-borne data. *Measurement* **189**, 110453 (2022).
3. Xu, W., Yan, C. & Chen, J. Performance evaluation of BDS-2/BDS-3 combined precise time transfer with B1I/B2I/B3I/B1C/B2a five-frequency observations. *Gps Solut.* **26**(3), 80 (2022).
4. Zhao, X. *et al.* Research on the impact of BDS-2/3 receiver ISB on LEO satellite POD. *Remote Sens.* **14**(11), 2514 (2022).
5. Doberstein, D. *Fundamentals of GPS Receivers* 203–318 (Springer, 2012).
6. Zhou, H. *et al.* Real-time GNSS triple-frequency cycle slip detection using three optimal linear combinations. *Gps Solut.* **27**(3), 142 (2023).
7. Miao, Y., Sun, Z. & Wu, S. Error analysis and cycle-slip detection research on satellite-borne GPS observation. *J. Aerospace Eng.* **24**(1), 95–101 (2011).
8. Xu, X. F., Nie, Z. X., Wang, Z. J. & Zhang, Y. F. A modified turboedit cycle-slip detection and correction method for dual-frequency smartphone GNSS observation. *Sensors* **20**(20), 5756 (2020).
9. Dong, Y. *et al.* A study on the detecting cycle slips and a repair algorithm for B1/B3. *Electronics* **10**(23), 2925 (2021).
10. Ye, S., Yan, Y. & Chen, D. Performance analysis of velocity estimation with BDS. *J. Navig.* **70**(3), 580–594 (2017).
11. Wang, X., Tu, R., Gao, Y., Zhang, R. & Lu, X. Velocity estimations by combining time-differenced GPS and Doppler observations. *Meas. Sci. Technol.* **30**(12), 125003 (2019).

12. Gao, Y. & Zhang, Y. Pseudo-range phase method combined with ultra long wavelength combination detection and repair cycle slip. *GNSS World China* **43**(02), 28–32 (2018).
13. Cai, C. S., Liu, Z. Z., Xia, P. F. & Dai, W. J. Cycle slip detection and repair for undifferenced GPS observations under high ionospheric activity. *Gps Solut.* **17**(2), 247–260 (2013).
14. Cai, C. *et al.* Cycle slip detection and repair for undifferenced GPS observations under high iono-spheric activity. *Gps Solut.* **17**(2), 247–260 (2013).
15. Chen, D. *et al.* A double-differenced cycle slip detection and repair method for GNSS CORS network. *Gps Solut.* **20**(3), 439–450 (2016).
16. Wang, H., Chai, H. & Xie, K. Study of cycle-slip detection using BDS triple-frequency geometry-free and lonosphere-free combination. *J. Geod. Geodyn.* **35**(03), 406–411 (2015).
17. Huang, L. *et al.* A new triple-frequency cycle slip detecting algorithm validated with BDS data. *GPS Solut.* **20**, 761–769 (2016).
18. Xiong, Y. L., Huang, D. F. & Shum, C. K. GPS phase measure cycle-slip detecting and GPS baseline resolution based on wavelet transform. *Surv. Rev.* **37**(289), 200–207 (2003).
19. Lacy, M. C. D., Reguzzoni, M., Sanso, F. & Venuti, G. The Bayesian detection of discontinuities in a polynomial regression and its application to the cycle-slip problem. *J. Geod.* **82**(9), 527–542 (2008).
20. Zangeneh-Nejad, F., Amiri-Simkooei, A. R., Sharifi, M. A. & Asgari, J. Cycle slip detection and repair of undifferenced single-frequency GPS carrier phase observations. *GPS Solut.* **21**, 1593–1603 (2017).
21. Yin, L., Li, S., Deng, Z. & Zhu, D. A novel cycle slips detection model for the high precision positioning. *IEEE Access* **7**, 24041–24050 (2019).
22. Huo, G. P. & Miao, L. J. Cycle-slip detection of GPS carrier phase with methodology of SA4 multi-wavelet transform. *Chin. J. Aeronaut.* **25**(2), 227–235 (2012).
23. Zhang, W. & Wang, J. A real-time cycle slip repair method using the multi-epoch geometry-based model. *Gps Solut.* **25**(2), 60 (2021).
24. Dong, B., Chai, H., Li, M. & Wang, M. A new cycle slip detection and correction method with dual-frequency carrier phase observation and high-order difference. *Hydrograph. Surv. Chart.* **36**(02), 58–62 (2016).
25. Chen, Y. *Research on GPS Cycle Slip Detection and Repairing Problem* (Chang'an University, 2014).
26. Chang, G., Xu, T., Yao, Y. & Wang, Q. Adaptive Kalman filter based on variance component estimation for the prediction of ionospheric delay in aiding the cycle slip repair of GNSS triple-frequency signals. *J. Geod.* **92**(11), 1241–1253 (2018).
27. Liu, W. *et al.* An improved robust Kalman filtering strategy for GNSS kinematic positioning considering small cycle slips. *Adv. Space Res.* **63**(9), 2724–2734 (2019).
28. Cai, C., Wang, L., Wang, J., Qin, Y. & Li, G. lmprovement of lonosphere residual method in carrier phase cycle-slip detection. *Telecommun. Eng.* **56**(5), 551–556 (2016).
29. Liu, N., Zhang, Q., Zhang, S. & Wu, X. Algorithm for real-time cycle slip detection and repair for low elevation GPS undifferenced data in different environments. *Remote Sens.* **13**(11), 2078 (2021).
30. Feng, Y. *Fast Cycle Slip Determination for High-Rate Multi-GNSS RTK Using Modified Geometry-Free Phase Combination* (Northwest University, 2020).
31. Zhang, C., Dang, Y., Wang, X., Quan, J. & Yu, Z. A real-time cycle slip detection and repair method based on ionospheric delay prediction for undifferenced triple-frequency BDS signals. *IEEE Access* **9**, 69999–70013 (2021).
32. Zhang, F., Liu, C., Feng, X., Li, L. & Wang, F. A triple-frequency cycle slip real-time processing method for BDS based on extented ridge estimation. *Geomat. Inf. Sci. Wuhan Univ.* **45**(01), 62–71 (2020).
33. Zhao, Q. *et al.* Real-time detection and repair of cycle slips in triple-frequency GNSS measurements. *Gps Solut.* **19**(3), 381–391 (2015).
34. Li, B., Qin, Y. & Liu, T. Geometry-based cycle slip and data gap repair for multi-GNSS and multi-frequency observations. *J. Geod.* **93**(3), 399–417 (2019).

Acknowledgements

This work is funded by the National Natural Science Foundation of China (No. 41774039, 42204040), the State Key Lab Project of China (No. 6142210200104), the Key Project of Science and Technology of Henan (No. 212102210085) and the Fundamental Research Funds for the Universities of Henan Province (No.NSFRF210309). The authors would like to thank C.K, who is a professor at The Ohio State University, for providing the valuable advice.

Author contributions

H.B. designed the experiments and wrote the main manuscript. K.L. reviewed the manuscript. K.W. and L.L. collected all experimental raw measurements. Y.J. assisted in collecting experimental raw measurements. The experimental work is being established and maintained by Z.Y. and C.T. All components of this research were carried out under H.B. All authors reviewed the manuscript.

Competing interests

The authors declare no competing interests.

Additional information

Correspondence and requests for materials should be addressed to K.L.